ACS APPLIED MATERIALS & INTERFACES

Research Article

www.acsami.org

Self-Assembled Fe_2O_3/Graphene Aerogel with High Lithium Storage Performance

Li Xiao,[†,§] Dongqing Wu,[‡,§] Sheng Han,[‡] Yanshan Huang,[‡] Shuang Li,[‡] Mingzhong He,[†] Fan Zhang,*[,‡] and Xinliang Feng*[,‡,⊥]

[†]Faculty of Material Science and Chemistry, China University of Geosciences, Wuhan 430074, P. R. China

[‡]School of Chemistry and Chemical Engineering, Shanghai Jiao Tong University, Shanghai 200240, P. R. China

[⊥]Max Planck Institute for Polymer Research, Mainz 55128, Germany

Supporting Information

ABSTRACT: In this study, graphene aerogel (GA)-supported Fe_2O_3 particles with three-dimensional (3D) architecture was prepared by a one-pot hydrothermal process. Fe_2O_3 particles were dispersed uniformly on the graphene sheets, and the resulting composites self-assembled into a 3D network via hydrothermal treatment. This strategy provides a facile and environmentally friendly method for the large-scale synthesis of Fe_2O_3/GAs without any additional reductant. As the anode material for lithium ion batteries, the Fe_2O_3/GAs in this study manifested an excellent reversible capacity of 995 mA h g^{-1} after 50 cycles at a charge−discharge rate of 100 mA g^{-1} and even delivered reversible capacity as high as 372 mA h g^{-1} at a high rate of 5000 mA g^{-1}. The outstanding electrochemical performance of Fe_2O_3/GAs can be attributed to the synergistic interaction between uniformly dispersed Fe_2O_3 particles and graphene aerogel, in which a robust 3D framework of graphene provided highly conductive networks with a large surface area and short diffusion path length for the transport of lithium ions.

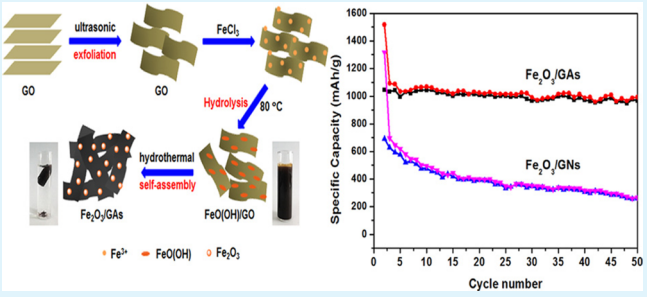

KEYWORDS: *Fe_2O_3/GAs, 3D interconnected graphene, self-assembly, anode material, lithium-ion batteries*

1. INTRODUCTION

Rechargeable lithium ion batteries (LIBs) have become one of the most promising type of battery technology for electrochemical energy storage due to their high energy density, low maintenance, and relatively low self-discharge.[1−3] However, in the classical commercial LIBs, graphitic carbon is the most popular anode material, which only delivers a theoretical specific capacity of 372 mA h g^{-1}.[4] Developing new electrode materials with high energy densities has been an important way to satisfy the ever-growing demand for high performance LIBs.[5−8] Nanostructured metal oxides (MOs) are regarded as potential anode materials for LIBs because of their various advantages, such as high reversible capacity, fast power capability, good safety, and long cycle life.[9−13] Among them, Fe_2O_3 has attracted much attention, owing to its appealing features, including high theoretical specific capacity (1005 mA h g^{-1}), natural abundance, low cost, and environmental friendliness.[14−18] Nevertheless, because of the low conductivity and strong agglomeration during the charge and discharge processes, Fe_2O_3 particles suffer from rapid capacity fading caused by volume changes and subsequent particle pulverization.[19−21] To overcome these obstacles, conducting carbon matrices have been introduced to absorb the volume changes and to improve the structural stability of the electrodes.[22−24] Graphene, a single−layer of sp^2 carbon lattices, has been considered as the one of the most appealing carbon matrices for MO particles because of its outstanding charge carrier mobility, mechanical robustness, and thermal and chemical stability.[25,26] More recently, it was revealed that the assembly of 2D graphene sheets into 3D architectures[27−29] can provide resultant graphene-based composites with strong mechanical strengths, and fast mass and electron transport kinetics due to the combination of the 3D interconnected framework and the intriguing properties of graphene.[30,31] Nevertheless, to the best of our knowledge, a study of Fe_2O_3 particles supported on 3D interconnected graphene as anode materials for LIBs has not been reported to date.

Herein, a novel class of monolithic 3D Fe_2O_3/GAs was fabricated via a combined hydrothermal self-assembly and freeze-drying process. Uniform Fe_2O_3 particles and supporting graphene networks were simultaneously synthesized through a hydrothermal procedure using $FeCl_3$ and 2D graphene oxide (GO) as the precursors. Compared with the Fe_2O_3 particles supported on 2D graphene sheets (Fe_2O_3/GNs), Fe_2O_3/GAs demonstrate 3D interconnected macroporous architecture with a uniform deposition of Fe_2O_3 particles, which provides highly

Received: January 29, 2013
Accepted: April 3, 2013
Published: April 3, 2013

conductive networks with enhanced surface areas and short diffusion path lengths for lithium ion transport. As a result, Fe_2O_3/GAs exhibit outstanding reversible capacity and excellent rate performance (995 mA h g^{-1} after 50 cycles at a charge−discharge rate of 100 mA g^{-1} and reversible discharging capacity 372 mA h g^{-1} at 5000 mA g^{-1}), when applied as the anode material for lithium storage.

2. EXPERIMENTAL SECTION

2.1. Materials. Graphite flakes were purchased from Sigma Aldrich (USA). $NaNO_3$, $KMnO_4$, 98% H_2SO_4, 30% H_2O_2, $FeCl_3{\cdot}6H_2O$, and $N_2H_4{\cdot}H_2O$ were purchased from Sinopharm Chemical Reagent Co. Ltd. (Shanghai, China). All chemicals were of analytical grade and were used as received without further purification.

2.2. Synthesis of Fe_2O_3/GAs. Graphene oxide (GO) was synthesized from natural graphite flakes using a modified Hummers method.[32,33] Exfoliation was carried out by ultrasonicating the GO dispersion under ambient conditions. For the preparation of Fe_2O_3/GAs, 40 mL of a 1 mg mL^{-1} GO suspension was ultrasonicated for 0.5 h, into which 10 mL of 0.1 mol L^{-1} $FeCl_3$ solution was added slowly. The mixture was heated to 80 °C and kept at this temperature for 5 h. The resulting suspension was collected by centrifugation, washed repeatedly with deionized water, and then, the obtained hydrogel was dispersed in 20 mL of deionized water in a 25 mL cylindrical vessel. Subsequently, the cylindrical vessel was sealed in a 50 mL Telfon-lined autoclave and hydrothermally treated at 180 °C for 12 h. Next, the as-prepared sample was freeze-dried overnight. As a control experiment, reduced graphene oxide (RGO) aerogel was prepared in the absence of $FeCl_3$ via a similar procedure, and bare Fe_2O_3 particles were also synthesized without adding GO. For comparison, Fe_2O_3/GNs were synthesized by physically mixing Fe_2O_3 particles with RGO. In detail, 40 mL of a 1 mg mL^{-1} GO suspension was reduced by 125 μL $N_2H_4{\cdot}H_2O$ at 90 °C for 1 h. When cooled to room temperature, a 0.5 mmol portion of Fe_2O_3 particles was added to the mixture under ultrasonication for 0.5 h and vigorous stirring for 12 h. The resulting suspension was centrifuged and washed with deionized water three times. Finally, the Fe_2O_3/GNs were obtained by drying the precipitations at 60 °C for 12 h.

2.3. Materials Characterizations. The morphology of the samples was investigated by field−emission scanning electron microscope (FESEM, FEI, Sirion 200) and transmission electron microscope (TEM, JEOL, JEM−2010). Raman spectra were recorded on a Senterra R200-L multichannel confocal microspectrometer with 532 nm laser excitation. The X-ray photoelectron spectrum (XPS) was conducted on an X-ray photoelectron spectrometer using a Mg−Kα radiation exciting source (AXIS ULTRA DLD, Kratos). The materials were also characterized by powder X-ray diffraction (XRD) using a Rigaku X-ray diffractometer with Cu−Kα irradiation (λ = 0.15406 nm) at 40 kV, 20 mA over the 2θ range from 10 to 70°. Thermogravimetric analysis (TGA) was measured by a TA Q5000IR with a heating rate of 20 °C min^{-1} under flowing air. Nitrogen adsorption/desorption isotherms at 77 K were determined by Micromeritics ASAP 2010.

2.4. Electrochemical Measurements. The electrochemical properties of the samples were evaluated with CR 2016 coin cells. The test electrodes were prepared by mixing active materials with conductive carbon black (super P) as the conductive agent and polyvinylidene fluoride (PVDF) dissolved in *N*-methyl-2-pyrrolidone (NMP) as the binder in a weight ratio of 80:10:10 to form a slurry, which was then coated onto a copper foil. The mass of active material on each anode was ca. 1.0 mg. Pure lithium foils were used as counter electrodes. A Celgard 2400 microporous polypropylene membrane was used as a separator. The electrolyte consisted of a solution of 1 M $LiPF_6$ in ethylene carbonate−dimethyl carbonate−diethyl carbonate (1:1:1, in weight percent). CR 2016 coin cells were assembled in an argon−filled glovebox with water and oxygen contents less than 1 ppm. The discharge and charge measurements were carried on a LAND 2001A system with the cutoff potentials being 0.01 V for discharge and 3.0 V for charge. Electrochemical impedance spectroscopy (EIS) was performed on a CHI760D electrochemical workstation by applying a sine wave with an amplitude of 0.5 mV in the frequency range 100 kHz to 0.01 Hz.

3. RESULTS AND DISCUSSION

The synthetic route to Fe_2O_3/GAs is schematically illustrated in Scheme 1. First, Fe^{3+} cations from $FeCl_3$ can favorably bind

Scheme 1. Schematic Illustration of the Synthesis Route to 3D Fe_2O_3/GAs

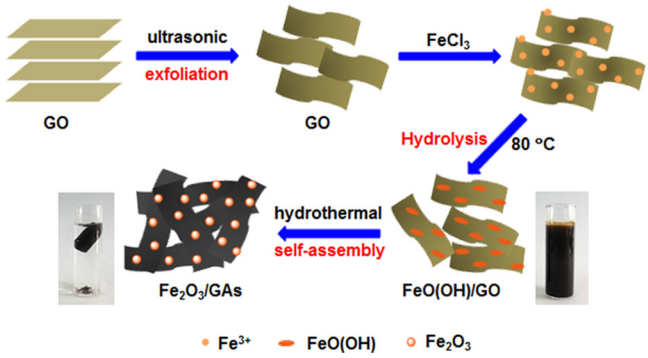

with oxygen-containing groups on GO sheets via electrostatic interactions. Second, upon heating the mixture to 80 °C, the hydrolysis of Fe^{3+} leads to the formation of FeO(OH) (Supporting Information, Figure S1) deposited on the surface of the GO sheets. Third, 2D GO sheets with a uniform decoration of FeO(OH) act as a building block and self-assemble into 3D monolithic networks by hydrothermal treatment. The GO is simultaneously transformed into RGO, and the FeO(OH) is transformed into Fe_2O_3 during this step. Finally, light black Fe_2O_3/GAs are obtained after the freeze-drying process.

The morphology and microstructure of the as-prepared Fe_2O_3/GAs were elucidated by means of FESEM, TEM, and nitrogen adsorption/desorption analysis. FESEM images of a cross-section of Fe_2O_3/GAs (Figure 1c) clearly showed that the Fe_2O_3 particles featured a size of 50−200 nm anchored uniformly on both sides of the graphene sheets. It is noteworthy that some Fe_2O_3 particles can be encapsulated within the graphene sheets, which can efficiently prevent the aggregation of particles and avoid direct contact between Fe_2O_3 particles and electrolyte. The results also revealed GA as a rather thin, well-defined, and interconnected 3D network microstructure with uniformly dispersed pores of several micrometers in diameter, suggesting efficient assembly between the particles and graphene sheets during the hydrothermal treatment. Such a geometric confinement of MOs particles within graphene layers has been reported to enhance their interface contact and to suppress the dissolution and agglomeration of particles, thereby promoting the electrochemical activity and stability of the composites.[31] In contrast to Fe_2O_3/GAs with 3D porous frameworks, Fe_2O_3/GN exhibits a typical 2D sheetlike morphology with condensed packing (Supporting Information, Figure S5a and b). A high-resolution TEM (HRTEM) image of Fe_2O_3/GAs (Figure 1d) revealed typical regular lattice fringes with a *d* spacing of 0.25 nm, corresponding to the (110) planes of Fe_2O_3.[34] A Brunauer−Emmett−Teller (BET) analysis of nitrogen adsorption/desorption isotherms revealed that the specific surface area of Fe_2O_3/GAs was 77 m^2 g^{-1}, which was much higher than that of bare Fe_2O_3, and the pore volume was 0.29 cm^3 g^{-1} for Fe_2O_3/

dx.doi.org/10.1021/am400387t | ACS Appl. Mater. Interfaces 2013, 5, 3764−3769

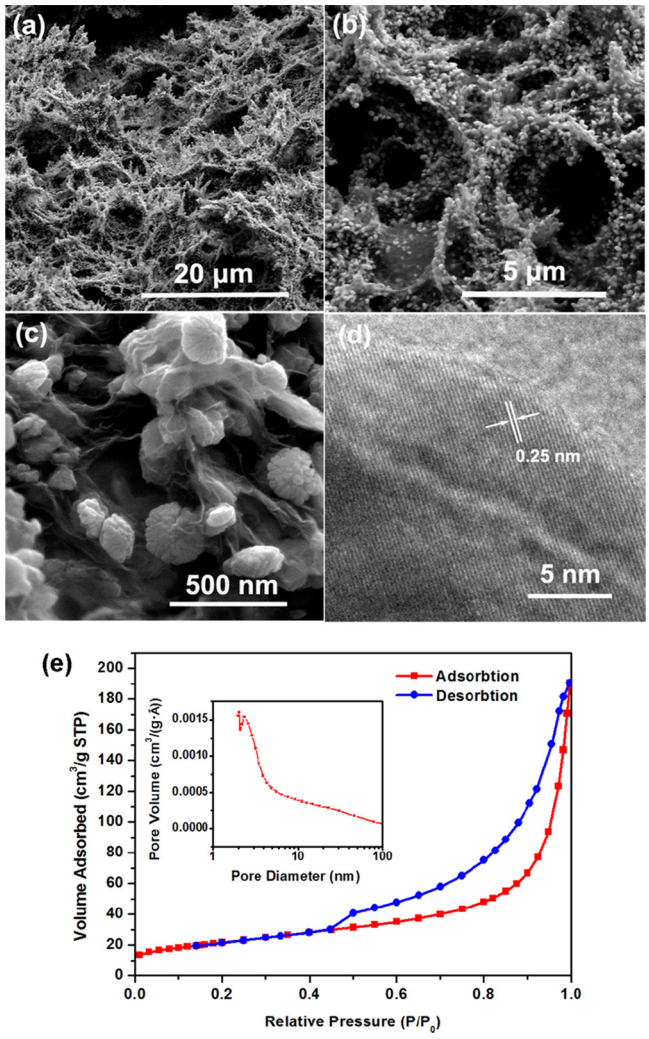

Figure 1. (a–c) Typical SEM images of Fe_2O_3/GAs revealing the 3D macroporous structure and uniform distribution of Fe_2O_3 particles. (d) HRTEM images of Fe_2O_3/GAs revealing Fe_2O_3 particles encapsulated by graphene sheets. (e) Nitrogen adsorption/desorption isotherms and pore size distribution of Fe_2O_3/GAs.

GAs (Figure 1e). Moreover, the pore size distribution calculated by the Barret–Joyner–Halenda (BJH) method ranged from 2.0 to 100 nm (inset in Figure 1e).

TGA measurement carried out in the air was used to determine the chemical composition of Fe_2O_3/GAs. As shown in Figure 2a, the TGA curve displays a significant weight loss at approximately 450 °C and a constant weight above 500 °C. The miniscule weight loss (<2%) that appeared below 300 °C is most likely attributed to the evaporation of adsorbed water molecules.[29] The major weight loss from 300 to 500 °C was approximately 20%, indicating the combustion of graphene. Therefore, the content of Fe_2O_3 in Fe_2O_3/GAs was calculated to be 78%. The crystal structure of the final products was identified by XRD measurement. The XRD pattern of Fe_2O_3/GAs corresponds to the upper profile in Figure 2b, and all the peaks can be assigned to Fe_2O_3 (JCPDS No. 33-0664). No apparent diffraction peak at 26° corresponding to graphene was observed in the pattern of the Fe_2O_3/GAs.

Raman spectra of GO, GAs and Fe_2O_3/GAs are shown in Figure 2c. All three samples show fairly strong D bands (the A_{1g} symmetry mode) in the vicinity of 1338 cm^{-1} and G bands (the E_{2g} mode of the sp^2 carbon atoms) in the vicinity of 1596 cm^{-1}.[35] The intensity ratio of D/G bands for GO and GAs is 0.92 and 1.00, respectively, while it is increased to 1.04 for Fe_2O_3/GAs. The difference in the D/G ratio suggests an increase in the number of sp^2 domains in GAs and Fe_2O_3/GAs, confirming the reduction of GO.[36,37] On the other hand, given by the XPS spectrum of core-level C1s for GO and Fe_2O_3/GAs in Figure 2d, the reduction of GO during the hydrothermal process is also validated by the significant intensity enhancement for sp^2 C=C bonds at 284.6 eV and the decrease of the epoxy C—O bonds at 286.6 eV.[38]

Galvanostatic discharge (Li insertion)–charge (Li extraction) measurements were carried out at a current density of 100 mA g^{-1} over a voltage range from 0.01 to 3.0 V to evaluate the electrochemical performance of the as-prepared Fe_2O_3/GAs. The first lithium insertion profile could be divided into three stages: $Fe_2O_3 \rightarrow Li_xFe_2O_3 \rightarrow$ cubic $Li_2Fe_2O_3 \leftrightarrow Fe + Li_2O$. At the early stage of lithium insertion (plateau I), a small amount of lithium was inserted into the crystal structure of Fe_2O_3 before the structural transformation of the close-packed anionic array from hexagonal to cubic stacking occurred. During the following stage of lithium insertion (plateau II), a similar profile as plateau I was found. And a long plateau III appeared at approximately 0.80 V, corresponding to a reversible reaction between cubic $Li_2Fe_2O_3$ and Fe in the third stage.[39–41] The first discharge/charge step delivered a specific discharge capacity of 1515 mA h g^{-1} and charge capacity of 1045 mA h g^{-1} (the value of capacity is based on the total mass of the Fe_2O_3/GAs) with initial Coulombic efficiency of 69% (Figure 3a). This initial capacity loss could potentially be attributed to the formation of a solid electrolyte interphase (SEI) layer on the electrode surface during the first discharge step. At the end of 50 charge–discharge cycles, a reversible capacity as high as 995 mA h g^{-1} could still be retained (Figure 3c), which was much higher than the theoretical specific capacity of graphene (372 mA h g^{-1}). As a comparison, physically mixed Fe_2O_3/GNs demonstrated a much lower first-cycle discharge capacity of 1316 mA h g^{-1}, and the capacity dropped quickly to 263 mA h g^{-1} after 50 cycles (Figure 3c). The rate performances of Fe_2O_3/GAs at the current rates of 100–5000 mA g^{-1} are depicted in Figure 3d. Reversible capacities were retained at 756 and 624 mA h g^{-1} at 1000 and 2000 mA g^{-1}, respectively, and the Coulombic efficiencies were close to 98%. Remarkably, a reversible capacity of 372 mA h g^{-1} could still be delivered at a very high rate of 5000 mA g^{-1}. SEM images of Fe_2O_3/GNs after cycling (Supporting Information, Figure S5c and d) suggest that Fe_2O_3 particles on Fe_2O_3/GNs exhibit obvious pulverization and aggregation after 50 cycles. In contrast, Fe_2O_3 particles on Fe_2O_3/GAs after cycling (Supporting Information, Figure S4) do not suffer from distinct morphological change and maintain the uniform distribution on graphene sheets. Such a prominent difference between Fe_2O_3/GAs and Fe_2O_3/GNs emphasizes the efficiency of our protocol to improve the electrochemical performance of Fe_2O_3 by incorporation of 3D graphene aerogel. Moreover, the stable cycle performance of Fe_2O_3/GAs at high rates indicated the ultrafast diffusion of lithium ions in bulk, owing to the short diffusion path length and the stable 3D graphene structure.

In order to gain insight into the remarkable rate performance of Fe_2O_3/GAs compared with Fe_2O_3/GNs, AC impedance spectra measurements were carried out. As demonstrated by the Nyquist plots in Figure 4a, the diameter of the semicircle for Fe_2O_3/GAs in the high-medium frequency region was much

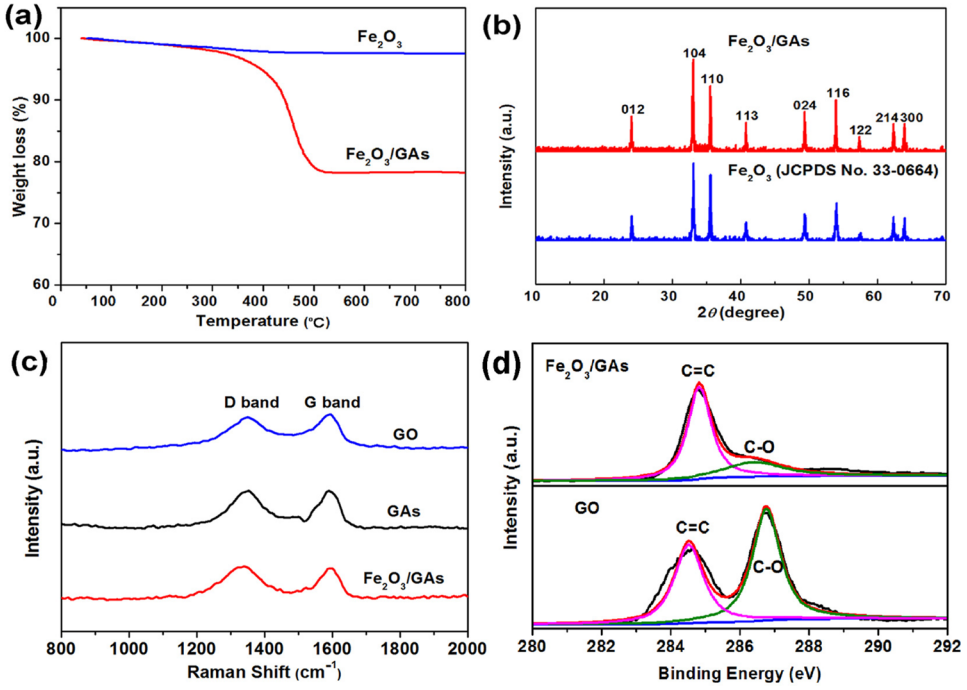

Figure 2. (a) TGA curves for Fe_2O_3 particles and Fe_2O_3/GAs in the air. (b) XRD patterns of Fe_2O_3/GAs and Fe_2O_3 particles. (c) Raman spectra of Fe_2O_3/GAs, GAs, and GO. (d) XPS spectra of core-level C1s for GO and Fe_2O_3/GAs.

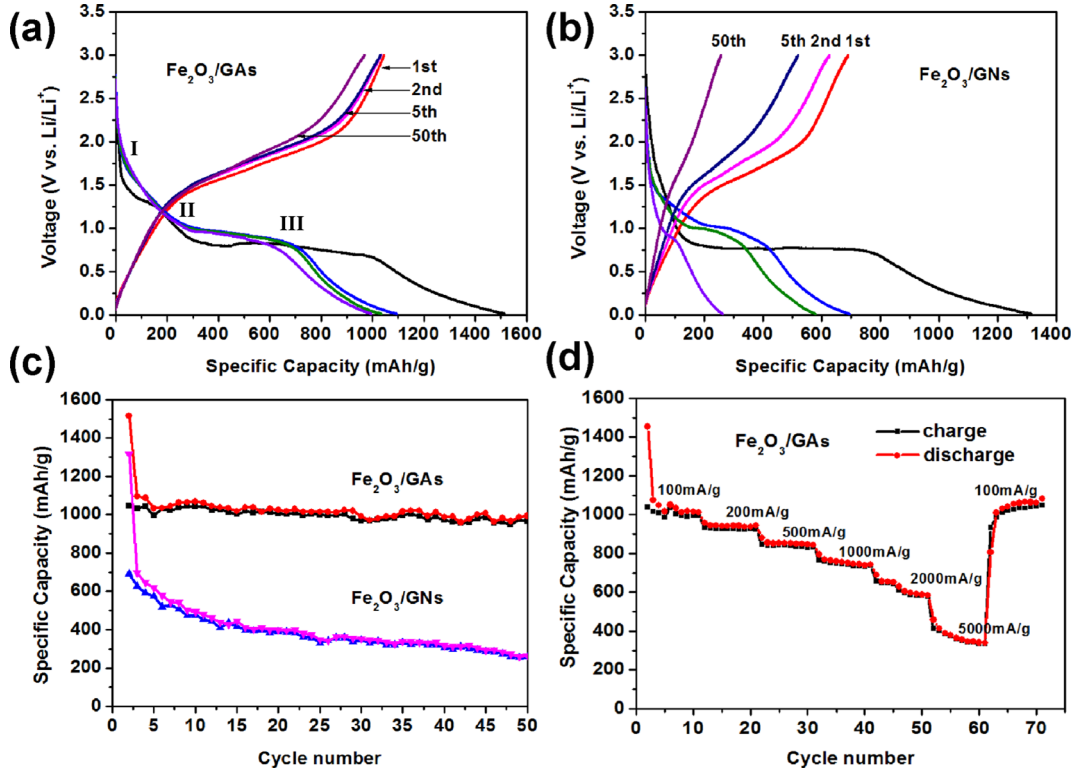

Figure 3. (a) Discharge/charge profiles of Fe_2O_3/GAs and (b) Fe_2O_3/GNs at the current density of 100 mA g^{-1} between 0.01 and 3.0 V: the discharge curves in the first, second, fifth, and 50th cycles. (c) Cycling performance of Fe_2O_3/GAs and Fe_2O_3/GNs at the current density of 100 mA g^{-1}. (d) Rate capacity of Fe_2O_3/GAs between 0.01 and 3.0 V with increasing current density.

smaller than that of Fe_2O_3/GNs, which suggested that Fe_2O_3/GAs possessed lower contact and charge−transfer resistances. The exact kinetic differences between Fe_2O_3/GAs and Fe_2O_3/GNs were inspected by modeling AC impedance spectra based on the modified Randles equivalent circuit (Figure 4b) and are summarized in Table 1.[42,43] It can be seen that the values of SEI film resistance R_f and charge−transfer resistance R_{ct} of the Fe_2O_3/GAs electrode are 265.8 and 52.8 Ω, respectively, which were observed to be significantly lower than those of Fe_2O_3/GNs (656.8 and 95.0 Ω, respectively). This result validated that

dx.doi.org/10.1021/am400387t | ACS Appl. Mater. Interfaces 2013, 5, 3764−3769

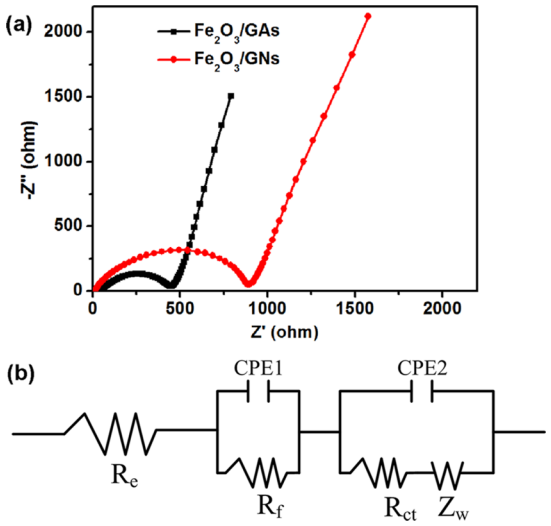

Figure 4. (a) Nyquist plots of Fe_2O_3/GAs and Fe_2O_3/GNs obtained by applying a sine wave with an amplitude of 5.0 mV over the frequency range from 100 kHz to 0.01 Hz. (b) Randles equivalent circuit for Fe_2O_3/GAs and Fe_2O_3/GNs electrode/electrolyte interface. R_e is the electrolyte resistance, and R_f is the resistance of the surface film formed on the electrodes. R_{ct} is charge−transfer resistance, Z_w is the Warburg impedance related to the diffusion of lithium ions in the bulk electrodes, and CPE represents the constant phase element, $Z_{CPE} = \{Q(j\omega)n\}^{-1}$, $0 \leq n \leq 1$.

Table 1. Kinetic Parameters of Fe_2O_3/GAs and Fe_2O_3/GNs Electrodes

samples	R_f (Ω)	Q_1 (μF)	R_{ct} (Ω)	Q_2 (μF)
Fe_2O_3/GAs	265.8	5.0	52.8	9.0
Fe_2O_3/GNs	656.8	1.2	95.0	0.5

the 3D graphene architecture in Fe_2O_3/GAs not only improved the high conductivity of the overall electrode but also largely enhanced the electrochemical activity during the cycle processes.

The high capacity, good cycling stability, and excellent rate capability of Fe_2O_3/GAs observed can be attributed to synergistic interactions between Fe_2O_3 particles and graphene aerogel associated with a 3D interconnected macroporous framework.[29,31,38] First, the 3D graphene networks provide a large surface area and efficiently reduce the diffusion length for both electrons and lithium ions. Second, the conductive graphene sheets with 3D frameworks can serve as multidimensional pathways to facilitate the transport of electrons in the bulk electrode. Third, some Fe_2O_3 particles were encapsulated within the graphene sheets, which thus can suppress the aggregation of Fe_2O_3 particles and accommodate their volume expansion during the cycling.

4. CONCLUSIONS

In summary, 3D monolithic Fe_2O_3/GAs were successfully fabricated via a one-pot hydrothermal reaction and subsequent freeze-drying process. When the resulting 3D Fe_2O_3/GAs were applied as LIBs anodes, they demonstrated outstanding enhancement of durability and rate performance compared with Fe_2O_3/GNs, with a very high reversible capacity of 995 mA h g^{-1}, even after 50 cycles and 372 mA h g^{-1} at a high rate of 5000 mA g^{-1}. It is believed that our present synthetic strategy can be further extended to develop other graphene-based MOs monoliths as high performance electrode materials in LIBs with high specific capacities and rate capabilities.

■ ASSOCIATED CONTENT

Supporting Information

TEM image and XRD pattern of FeO(OH)/GO. SEM images, nitrogen adsorption/desorption isotherm, and pore size distribution of GAs. SEM images of the bare Fe_2O_3 particles. SEM images of the Fe_2O_3/GAs after 50 discharge/charge cycles. SEM images of Fe_2O_3/GNs after 50 discharge/charge cycles. This material is available free of charge via the Internet at http://pubs.acs.org.

■ AUTHOR INFORMATION

Corresponding Author

*E-mail: fan-zhang@sjtu.edu.cn (F.Z.); feng@mpip-mainz.mpg.de (X.F.). Tel./Fax: +86-21-54748964.

Author Contributions

§L.X. and D.W.: These authors contributed equally to this work.

Notes

The authors declare no competing financial interest.

■ ACKNOWLEDGMENTS

We acknowledge funding support from 973 Program of China (2012CB933404), Natural Science Foundation of China (21174083 and 21102091), BASF, Shanghai Pujiang Program (11PJ1405400), and the Ph.D. Programs Foundation of Ministry of Education of China for Young Scholars (20110073120039).

■ REFERENCES

(1) Liu, D. W.; Cao, G. Z. *Energy Environ. Sci.* **2010**, *3*, 1218−1237.
(2) Luo, B.; Liu, S. M.; Zhi, L. J. *Small* **2012**, *8*, 630−646.
(3) Bruce, P. G.; Scrosati, B.; Tarascon, J−M. *Angew. Chem., Int. Ed.* **2008**, *47*, 2930−2946.
(4) Zhang, W. Y.; Zeng, Y.; Xiao, N.; Hng, H. H.; Yan, Q. Y. *J. Mater. Chem.* **2012**, *22*, 8455−8461.
(5) Thackeray, M. M.; Wolverton, C.; Isaacs, E. D. *Energy Environ. Sci.* **2012**, *5*, 7854−7863.
(6) Szczech, J. R.; Jin, S. *Energy Environ. Sci.* **2011**, *4*, 56−72.
(7) Yoon, S.; Liao, C.; Sun, X. G.; Bridges, C. A.; Unocic, R. R.; Nanda, J.; Dai, S.; Paranthaman, M. P. *J. Mater. Chem.* **2012**, *22*, 4611−4614.
(8) Chen, D.; Tang, L. H.; Li, J. H. *Chem. Soc. Rev.* **2010**, *39*, 3157−3180.
(9) Wu, H. B.; Chen, J. S.; Hng, H. H.; Lou, X. W. *Nanoscale* **2012**, *4*, 2526−2542.
(10) Ji, L. W.; Lin, Z.; Alcoutlabi, M.; Zhang, X. W. *Energy Environ. Sci.* **2011**, *4*, 2682−2699.
(11) Wang, H. L.; Cui, L. F.; Yang, Y.; Casalongue, H. S.; Robinson, J. T.; Liang, Y. Y.; Cui, Y.; Dai, H. J. *J. Am. Chem. Soc.* **2010**, *132*, 13978−13980.
(12) Wu, Z. S.; Ren, W. C.; Wen, L.; Gao, L. B.; Zhao, J. P.; Chen, Z. P.; Zhou, G. M.; Li, F.; Cheng, H. M. *ACS Nano* **2010**, *4*, 3187−3194.
(13) Liang, Y. Y.; Schwab, M. G.; Zhi, L. J.; Mugnaioli, E.; Kolb, U.; Feng, X. L.; Müllen, K. *J. Am. Chem. Soc.* **2010**, *132*, 15030−15037.
(14) Jia, X.; Chen, J. J.; Xu, J. H.; Shi., Y. N.; Fan, Y. Z.; Zheng, M. S.; Dong, Q. F. *Chem. Commun.* **2012**, *48*, 7410−7412.
(15) Zhao, Y.; Li, J. X.; Ding, Y. H.; Guan, L. H. *Chem. Commun.* **2011**, *47*, 7416−7418.
(16) Wang, B.; Chen, J. S.; Wu, H. B.; Wang, Z. Y.; Lou, X. W. *J. Am. Chem. Soc.* **2011**, *133*, 17146−17148.
(17) Jang, B.; Park, M.; Chae, O. B.; Park, S.; Kim, Y.; Oh, S. M.; Piao, Y.; Hyeon, T. *J. Am. Chem. Soc.* **2012**, *134*, 15010−15015.

(18) Zhang, L.; Wu, H. B.; Madhavi, S.; Hng, H. H.; Lou, X. W. *J. Am. Chem. Soc.* **2012**, *134*, 17388−17391.
(19) Zou, Y. Q.; Kan, J.; Wang, Y. *J. Phys. Chem. C* **2011**, *115*, 20747−20753.
(20) Zhu, X. J.; Zhu, Y. W.; Murali, S.; Stoller, M. D.; Ruoff, R. S. *ACS Nano* **2011**, *5*, 3333−3338.
(21) Zhu, J. X.; Lu, Z. Y.; Oo, M. O.; Hng, H. H.; Ma, J.; Zhang, H.; Yan, Q. *J. Mater. Chem.* **2011**, *21*, 12770−12776.
(22) Su, Y. Z.; Li, S.; Wu, D. Q.; Zhang, F.; Liang, H. W.; Gao, P. F.; Cheng, C.; Feng, X. L. *ACS Nano* **2012**, *6*, 8349−8356.
(23) Li, Q. Q.; Zhang, S.; Dai, L. M.; Li, L. S. *J. Am. Chem. Soc.* **2012**, *134*, 18932−18935.
(24) Yang, L. C.; Liu, L. L.; Zhu, Y. S.; Wang, X. J.; Wu, Y. P. *J. Mater. Chem.* **2012**, *22*, 13148−13152.
(25) Wu, D. Q.; Zhang, F.; Liang, H. W.; Feng, X. L. *Chem. Soc. Rev.* **2012**, *41*, 6160−6177.
(26) Wu, D. Q.; Zhang, F.; Liu, P.; Feng, X. L. *Chem.−Eur. J.* **2011**, *17*, 10804−10812.
(27) Li, C.; Shi, G. Q. *Nanoscale* **2012**, *4*, 5549−5563.
(28) Pumera, M. *Energy Environ. Sci.* **2011**, *4*, 668−674.
(29) Chen, W. F.; Li, S. R.; Chen, C. H.; Yan, L. F. *Adv. Mater.* **2011**, *23*, 5679−5683.
(30) Wu, Z. S.; Winter, A.; Chen, L.; Sun, Y.; Turchanin, A.; Feng, X. L.; Müllen, K. *Adv. Mater.* **2012**, *24*, 5130−5135.
(31) Wu, Z. S.; Sun, Y.; Tan, Y. Z.; Yang, S. B.; Feng, X. L.; Müllen, K. *J. Am. Chem. Soc.* **2012**, *134*, 19532−19535.
(32) Hummers, W. S.; Offeman, R. E. *J. Am. Chem. Soc.* **1958**, *80*, 1339−1339.
(33) Liang, Y. Y.; Wu, D. Q.; Feng, X. L.; Müllen, K. *Adv. Mater.* **2009**, *21*, 1679−1683.
(34) Zhang, M.; Qu, B. H.; Lei, D. N.; Chen, Y. J.; Yu, X. Z.; Chen, L. B.; Li, Q. H.; Wang, Y. G.; Wang, T. H. *J. Mater. Chem.* **2012**, *22*, 3868−3874.
(35) Chen, M. X.; Zhang, C. C.; Li, X. C.; Zhang, L.; Ma, Y. L.; Zhang, L.; Xu, X. Y.; Xia, F. L.; Wang, W.; Gao, J. P. *J. Mater. Chem. A* **2013**, *1*, 2869−2877.
(36) Gu, Y.; Xu, Y.; Wang, Y. *ACS Appl. Mater. Interfaces* **2013**, *5*, 801−806.
(37) Sui, Z. Y.; Zhang, X. T.; Lei, Y.; Luo, Y. J. *Carbon* **2011**, *49*, 4314−4321.
(38) Cong, H. P.; Ren, X. C.; Wang, P.; Yu, S. H. *ACS Nano* **2012**, *6*, 2693−2703.
(39) Larcher, D.; Masquelier, C.; Bonnin, D.; Chabre, Y.; Masson, V.; Leriche, J. B.; Tarascon, J−M. *J. Electrochem. Soc.* **2003**, *150*, A133−A139.
(40) Larcher, D.; Bonnin, D.; Cortes, R.; Rivals, I.; Personnaz, L.; Tarascon, J−M. *J. Electrochem. Soc.* **2003**, *150*, A1643−A1650.
(41) Wu, X. L.; Guo, Y. G.; Wan, L. J.; Hu, C. W. *J. Phys. Chem. C* **2008**, *112*, 16824−16829.
(42) Yang, S. B.; Feng, X. L.; Müllen, K. *Adv. Mater.* **2011**, *23*, 3575−3579.
(43) Chang, K.; Chen, W. X. *ACS Nano* **2011**, *5*, 4720−4728.